ARTICLE   OPEN

Check for updates

Origami-inspired perovskite X-ray detector by printing and folding

Henning Mescher[1,2], Fabian Schackmar[1,2,3], Robert Huber [1], Helge Eggers[1,2,3], Marcus Zuber [4,5], Elias Hamann [4], Georg Gramlich[6], Julian Dangelmaier[1], Qiaoshuang Zhang [1], Andres Georg Rösch [1], Thomas Zwick[6], Gerardo Hernandez-Sosa [1,2,3], Ulrich W. Paetzold [1,2] and Uli Lemmer [1,2,3] ✉

X-ray detectors are of pivotal importance for the scientific and technological progress in a wide range of medical, industrial, and scientific applications. Here, we take advantage of the printability of perovskite-based semiconductors and achieve a high X-ray sensitivity combined with the potential of an exceptional high spatial resolution by our origami-inspired folded perovskite X-ray detector. The high performance of our device is reached solely by the folded detector architecture and does not require any photolithography. The design and fabrication of a foldable perovskite sensor array is presented and the detector is characterized as a planar and as a folded device. Exposed to $50\,kVp-150\,kVp$ X-ray radiation, the planar detector reaches X-ray sensitivities of $25-35\,\mu C/(Gy_{air}cm^2)$, whereas the folded detector achieves remarkably increased X-ray sensitivities of several hundred $\mu C/(Gy_{air}cm^2)$ and a record value of $1409\,\mu C/(Gy_{air}cm^2)$ at $150\,kVp$ without photoconductive gain. Finally, the potential of an exceptional high spatial resolution of the folded detector of more than 20 lp/mm under 150 kVp X-ray radiation is demonstrated.

INTRODUCTION

X-rays can penetrate objects that are non-transparent for visible light and can therefore be used for non-destructive examinations in medicine[1,2], industry[3,4], and science[5,6]. The low interaction probability of hard X-ray photons is a challenge for their efficient detection as thick absorber layers are needed. This is especially valid for direct conversion X-ray detectors in a classical planar device geometry that generally comprise a semiconductor material placed between a front and a back electrode. Large device thicknesses, on the other hand, might hamper efficient charge carrier collection due to competing trapping and recombination processes. Consequently, apart from fabrication-related limitations, the choice of the absorber thickness needs to balance a high X-ray absorption efficiency and a good charge collection.

Over the past years, perovskite-based semiconductors have emerged as direct conversion X-ray absorbers as they promise to combine an efficient X-ray absorption, a high conversion efficiency into charge carriers, and a good charge transport. Moreover, high-quality perovskite-based semiconductors can be deposited onto rigid as well as flexible substrates at low costs, e.g., by solution processing and printing methods. As a result, a variety of approaches to realize high-performance perovskite-based X-ray detectors has been reported[7–11]. In this context, it is important to note that perovskite-based semiconductors can also be used to realize various photodetectors[12–14]. In contrast to the typical layer scheme of a classical X-ray detector, we here follow an alternative strategy that is based on an origami-inspired folded device architecture. The fundamental idea of this approach is to realize detector pixels comprising relatively thin perovskite absorbers on top of a flexible substrate and subsequently create a folded device structure in which the radiation impinges parallel instead of perpendicular to the pixel electrodes. Consequently, a high X-ray absorption efficiency and therefore a high detection performance without the fabrication of excessively thick absorbers can be realized (c.f. Fig. 1). Furthermore, as the pixels of the folded detector are physically separated and their size can be controlled by the perovskite layer thickness, the folded layout promises to provide a high spatial resolution. Our work was stimulated by earlier work on edge-on configurations[15,16]. We take advantage of the processability of perovskite-based semiconductor thin films on mechanically flexible substrates to realize an origami-inspired folded X-ray detector. Our work is based on our previous studies in which we theoretically demonstrated the potential of the folded detector layout[17] and subsequently realized flexible perovskite X-ray detectors by digital inkjet printing[18].

In this study, we report on the realization of an origami-inspired folded perovskite X-ray detector. For this purpose, we present the fabrication of a foldable perovskite sensor array and characterize the detector's response to $50\,kVp-150\,kVp$ X-ray radiation before and after folding. Furthermore, we use a moving edge method to evaluate the potentially reachable spatial resolution of the folded perovskite X-ray detector. We finally investigate the operational stability of our device by measuring the detector's response under continuous X-ray radiation.

RESULTS AND DISCUSSION

Detector design and fabrication

The design of the detector foil and the manufacturing scheme from the planar to the origami-inspired folded detector is illustrated in Fig. 1a. The detailed device architecture of the

[1]Light Technology Institute (LTI), Karlsruhe Institute of Technology (KIT), Karlsruhe 76131, Germany. [2]Institute of Microstructure Technology (IMT), Karlsruhe Institute of Technology (KIT), Eggenstein-Leopoldshafen 76344, Germany. [3]InnovationLab (IL), Heidelberg 69115, Germany. [4]Institute for Photon Science and Synchrotron Radiation (IPS), Karlsruhe Institute of Technology (KIT), Eggenstein-Leopoldshafen 76344, Germany. [5]Laboratory for Applications of Synchrotron Radiation (LAS), Karlsruhe Institute of Technology (KIT), Karlsruhe 76131, Germany. [6]Institute of Radio Frequency Engineering and Electronics (IHE), Karlsruhe Institute of Technology (KIT), Karlsruhe 76131, Germany. ✉email: uli.lemmer@kit.edu
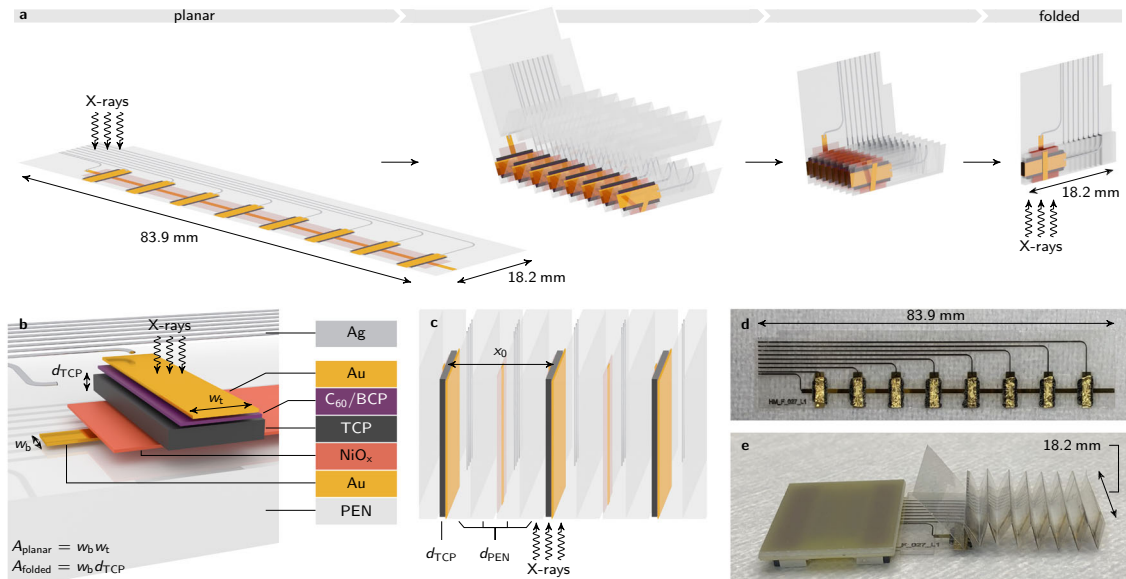
**Fig. 1 Planar and origami-inspired folded X-ray detector. a** Illustration of the folding process and the design of the perovskite X-ray detector in the planar and in the folded configuration. The respective orientation of the impinging X-ray radiation is additionally indicated. **b** Layer stack illustrated by an exemplary pixel in the planar configuration. A 25-μm-thick polyethylene naphthalate (PEN) foil serves as flexible substrate. Each pixel comprises thermally evaporated gold electrodes, a sputtered NiO_x hole transport layer, a 6-μm-thick inkjet-printed triple cation perovskite (TCP) absorber, and a thermally evaporated C_{60} fullerene and bathocuproine (BCP) electron transport layer. Aerosoljet-printed silver lines connect the pixel electrodes to the external read out electronics. The width of the bottom and top electrodes w_b and w_t, the thickness of the TCP absorber d_{TCP}, and the calculation of the effective pixel areas in the planar A_{planar} and in the folded configuration A_{folded} are additionally indicated. With a TCP absorber thickness of $d_{TCP} = 6\,\mu m$ and mean electrode widths of $\overline{w}_b = 1.02$ mm and $\overline{w}_t = 2.17$ mm, the mean effective pixel areas can be estimated as $\overline{A}_{planar} = 2.21\,mm^2$ and $\overline{A}_{folded} = 6.12 \times 10^{-3}\,mm^2$. **c** Section out of an exemplary pixel in the folded configuration. A second PEN foil serves as an additional protection layer. The dimensions of the TCP absorber d_{TCP}, the substrate d_{PEN}, and the pixel pitch of the folded detector x_0 are additionally indicated. The respective orientation of the X-ray beam in the planar (**b**) and in the folded configuration (**c**) emphasizes the reorientation of the TCP absorber within the X-ray beam by the folded detector design. **d**, **e** Photographs of the perovskite detector foil in the initial planar (**d**) and in an intermediate configuration (**e**).

detector is shown in Fig. 1b on the basis of an exemplary pixel in the planar configuration. The sensor array is fabricated on top of a flexible 25-μm-thick polyethylene naphthalate (PEN) foil. Each pixel of the detector is composed of a 6-μm-thick inkjet-printed triple cation perovskite (TCP, see Methods for the exact composition) absorber that is placed in between thermally evaporated gold electrodes. Based on our previous work on flexible perovskite X-ray detectors[18], additional hole transport layers of sputtered NiO_x and electron transport layers of thermally evaporated C_{60} fullerene and bathocuproine (BCP) are used as charge selective contacts. The electrical connection to the external read out electronics is realized by aerosoljet-printed silver lines (see Methods for fabrication details). In the planar configuration, as depicted in Fig. 1a, b, the perovskite sensor array is irradiated through the top gold electrodes and the X-ray absorption efficiency and therefore the detection performance is limited by the insufficient layer thickness of the TCP absorber. The fundamental idea of the folded device architecture is to fold the perovskite detector foil such that the TCP absorbers are reoriented within the X-ray beam, as illustrated in Fig. 1a. With a folding length of several mm, a sufficient absorption efficiency is reached. In order to ensure a precise folding of the detector foil, a laser cutter is used to engrave folding lines in the PEN foil prior to the device fabrication. A second PEN foil placed on top of the detector is utilized to prevent shunts and to protect the sensor array during the folding procedure. In the folded configuration, the X-ray radiation impinges under ideal circumstances parallel to the electrodes, as shown in Fig. 1c and the X-ray absorption efficiency depends no longer on the layer thickness but on the lateral dimension (folding length) of the TCP absorber. Consequently, the X-ray absorption efficiency within the active region of the folded detector is drastically increased. Furthermore, as the single pixels

of the folded detector are physically separated, charge-sharing effects between neighbouring pixels deteriorating the spatial resolution can be avoided. Note that issues such as K-edge X-ray fluorescence and Compton scattering remain and affect the spatial resolution of the folded detector.

As an alternative, we had considered to realize perovskite X-ray detectors in an edge-on geometry by stacking single-pixel detectors on top of each other. However, in the case of a stacked device, the connection to the external read out electronics and the alignment of the individual pixels is challenging. Furthermore, the device handling of multiple detectors that are realized on top of ultra-thin substrate foils, as it is required in our application, is difficult and impractical. The complexity regarding the connection to the external read out electronics, the pixel alignment, and the device handling of a stacked device increases with an increasing number of pixels. Consequently, the scalability of a stacked device is limited. In this context, the presented folded detector design has great advantages. A single flat cable is used to connect the folded detector to the external read-out electronics. The connection to the individual pixels is realized by printed silver lines and a shared bottom electrode that are processed directly on top of the detector foil. As a result of the laser-based engraving of the folding lines, the individual pixels are reliably aligned after the folding of the detector foil. Furthermore, compared to a stacked detector, only two ultra-thin substrate foils need to be handled. We therefore consider the here presented folded detector design more suited to be scaled to a larger number of pixels.

Figure 1d, e shows the perovskite detector foil in the initial planar and in an intermediate configuration (see Supplementary Fig. 1 for photographs of the detector in the planar and in the folded configuration clamped in the respective sample holder). The surface roughness of the pixels of our detector (see Fig. 1d)
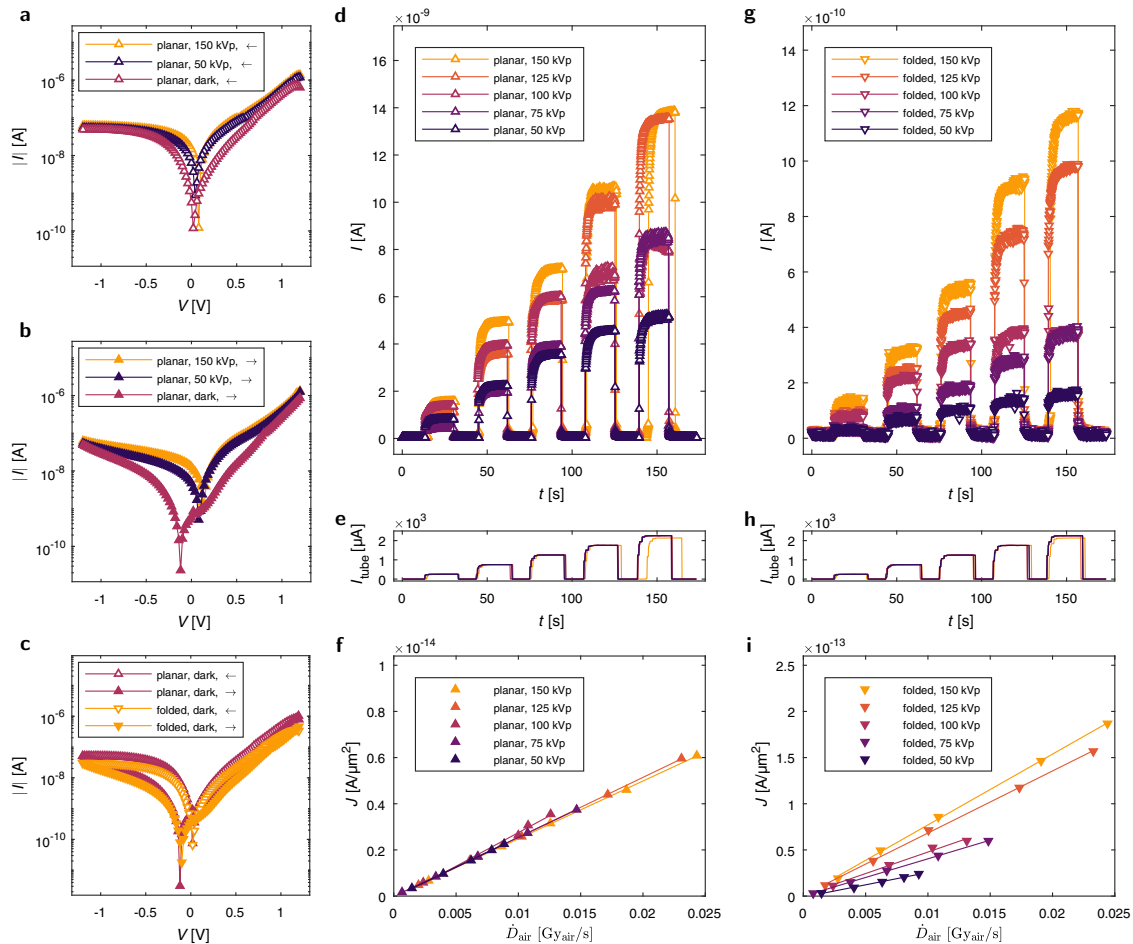
Fig. 2 Electrical characterization and X-ray sensitivity analysis. a, b Current–voltage characteristics (*I–V* curves) of the pixel in the planar configuration based on backward (**a**) and forward (**b**) voltage scanning. The *I–V* curves are measured in the dark, under 50 kVp, and under 150 kVp X-ray radiation. **c** Comparison of the *I–V* curves of the pixel measured in the initial planar and in the folded configuration. The arrows in the legend entries in (**a–c**) indicate the utilized voltage scanning direction. **d, g** Time-resolved current *I(t)* of the pixel in the planar and in the folded configuration under pulsed 50 kVp−150 kVp X-ray radiation. **e, h** Respective time-resolved X-ray tube current $I_{tube}(t)$ that is stepwise increased to realize different X-ray intensities at constant X-ray tube accelerating voltages. **f, i** Current densities *J* as a function of the applied dose rate in air $\dot{D}_{air}$ calculated from the measured pixel currents shown in (**d, g**). The results of the respective linear fits are additionally illustrated.

originates from drying effects of the printed TCP wet films (see Supplementary Fig. 9, Supplementary Fig. 10, and Supplementary Fig. 11 for a detailed characterization of the surface morphology of our devices).

Electrical characterization under different irradiation conditions

The electrical characterization and the X-ray sensitivity analysis of an exemplary pixel of the perovskite sensor array are presented in Fig. 2. The current–voltage characteristics (*I–V* curves) of the pixel in the initial planar configuration based on backward and forward voltage scanning are shown in Fig. 2a, b. The *I–V* curves are measured in the dark and under X-ray radiations with two different energy spectra. For this purpose, two X-ray tube accelerating voltages V_{tube} of 50 kVp and 150 kVp are used (see Supplementary Fig. 2 for the respective dose calibration). Independent of the voltage scanning direction and the irradiation conditions, the *I–V* curves show a clear diode blocking and transmission behaviour in reverse and forward bias, respectively. Furthermore, the X-ray photocurrent induced under 50 kVp and 150 kVp X-ray radiation compared to the measurement in the dark, demonstrates the capability of the device to detect X-ray

photons. Figure 2c shows a comparison of the *I–V* curves of the pixel measured in the initial planar and in the folded configuration. The slight differences between the *I–V* curves can be assigned to changes in the electrical resistance of the gold bottom electrode and the silver connections. We speculate that these changes orginate from mechanical stress caused by the folding of the device. Apart from these slight differences both measurements show nearly the same result. Consequently, the functionality of the pixel is not affected by the folding of the detector foil. The hysteresis of the *I–V* curves indicated in Fig. 2a–c is in accordance with the drifting dark currents that we observed in our previous study[18] and can be explained by slow ionic motions within the perovskite absorber. The relatively thin TCP absorbers used in our device enable a detector operation without high external bias. Combined with the utilized electron and hole transport materials, our detector can even be operated without any external bias. Thus, in order to minimize the impact of ion migrations and drifting dark currents, the X-ray characterization of the sensor array in this study is performed under zero bias (short circuit) conditions. The resulting time-resolved current *I(t)* of the pixel in the planar and in the folded configuration under 50 kVp −150 kVp X-ray radiation with varying dose rates (see Supplementary Fig. 3 for the respective dose calibration) is shown in
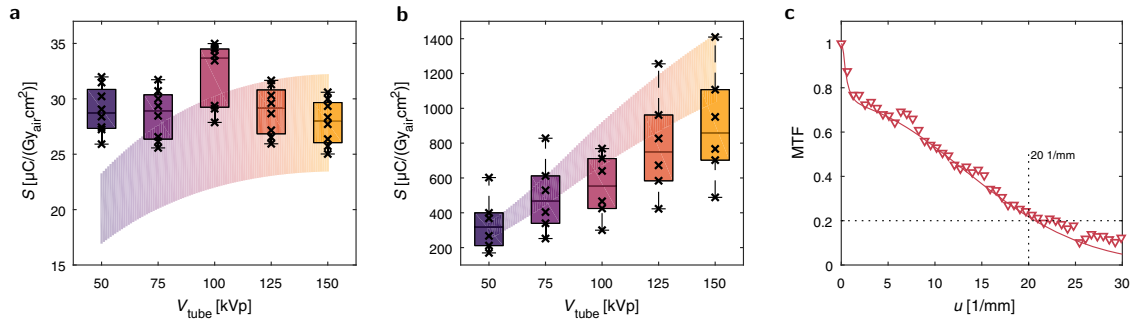
Fig. 3 X-ray sensitivity and spatial resolution. a, b X-ray sensitivities S of the planar (**a**) and the folded (**b**) detector as a function of the utilized X-ray tube voltage V_{tube}. The experimentally determined sensitivities are represented by box plots. The individual pixel sensitivities are also shown as symbols (crossed markers). The theoretical sensitivity prediction is depicted by the coloured areas. **c** Presampled modulation transfer function MTF of the folded detector as a function of the spatial frequency u. The MTF is determined by a numerical (markers) and an analytical (solid lines) approach.

Fig. 2d, g. The corresponding time-resolved X-ray tube current I_{tube} that is varied in order to realize different dose rates at constant X-ray tube accelerating voltages is additionally depicted in Fig. 2e, h. In both configurations a clear current response resolving the increasing intensity of the X-ray radiation is measured. In the planar configuration, the effective area is given by the overlapping area of the top and the bottom electrodes (see Fig. 1b), whereas in the folded configuration the effective area is significantly smaller as it is defined by the TCP absorber thickness and the lateral width of the gold bottom electrodes (see Fig. 1b, c). In a meaningful evaluation of detector responses, the respective effective areas need to be considered. For this reason, we follow the common approach and evaluate the detection performance of our detector by the X-ray sensitivity $S = Q/(D_{air}A)$ relating the induced charge Q with the X-ray dose in air D_{air} and the area A[19] that can be experimentally determined by the ratio of the current density J and the dose rate in air $\dot{D}_{air}$:

$$S_{exp} = \frac{J}{\dot{D}_{air}}. \qquad (1)$$

For this purpose, we determine the current densities J by normalizing the dark current corrected pixel currents to the respective effective area. The resulting current densities J as a function of the dose rate in air $\dot{D}_{air}$ of the incoming X-ray radiation are shown in Fig. 2f, i. The respective current densities show a drastically superior detector response in the folded configuration. In both pixel orientations, the measured current densities J under irradiation with a specific X-ray energy spectrum show a linear dependence on the dose rate in air $\dot{D}_{air}$ and the respective X-ray sensitivities S_{exp} can be determined by the slope of a linear fit.

X-ray sensitivity
The results of the X-ray sensitivity analysis are summarized in Fig. 3a, b. For this purpose, the experimentally determined sensitivities are represented by box plots with the underlying individual pixel sensitivities shown as crossed markers. As expected, the performance of the detector in the planar configuration is limited by the relatively thin TCP absorber and the measured X-ray sensitivities are in the range of $25-35\,\mu C/(Gy_{air}cm^2)$ (see Fig. 3a). In contrast, the folded detector shows a strong sensitivity improvement compared to the planar device with X-ray sensitivities in the order of several hundred $\mu C/(Gy_{air}cm^2)$ and a record value of $1409\,\mu C/(Gy_{air}cm^2)$ at 150 kVp (see Fig. 3b). Additionally, the folded detector shows an increased variation in the measured sensitivities. We speculate that this increased sensitivity variation is mainly caused by the actual orientation of the individual folded pixels within the X-ray beam.

Besides the pixel orientation, changes in the electrical resistance of the gold bottom electrode and the silver connections due to the folding might also influence the measured sensitivity variations. A variety of promising high-performance direct conversion X-ray detectors with sensitivities higher than $10^6\,\mu C/(Gy_{air}cm^2)$ have recently been published[7–9,20]. However, in most of these approaches, the exceptional high X-ray sensitivities presumably rely on photoconductive gain[7]. As we operate our detector at zero bias voltage, this effect should be negligible in our device. For a quantitative analysis of the behaviour of our detector, the measured X-ray sensitivities in Fig. 3a, b are compared to the theoretically expected performance assuming a device without gain (see coloured areas in Fig. 3a, b and see "Methods" for details on our sensitivity model). In the case of the planar configuration, the experimentally and the theoretically determined sensitivities show a good agreement. For high X-ray tube voltages we observe an excellent agreement while the experimental sensitivities are slightly higher than the theoretical prediction for lower X-ray energies. In the case of the folded detector, the experimentally determined performances show a good agreement with the theoretical prediction for low X-ray tube voltages and slightly lower sensitivities towards higher X-ray energies. Though, both the experimental and the theoretical evaluation in the case of the folded device assumes perfectly aligned pixels in a parallel X-ray beam. Deviations from this ideal situation (see Supplementary Fig. 4 for an evaluation of the pixel alignment by computed tomography slices) increase the effective pixel area and decrease the effective length within the TCP absorber along which X-ray photons can be absorbed. This would reduce the experimentally and the theoretically determined sensitivities and might explain the slight deviations at higher X-ray energies shown in Fig. 3b. The absence of photoconductive gain is also in accordance with the architecture of our devices as charge carrier injection, needed for photoconductive gain, should be suppressed by the utilized NiO_x and C_{60}/BCP barriers layers. Consequently, the here presented folded detector pushes the limits for the intrinsic (gain-free) X-ray sensitivity. We foresee a possible enhancement of the measurable signals and therefore also of the sensitivities by combining our folded architecture with photoconductive gain effects that could potentially be reached with other materials. It should be noted that by normalizing the detector signals to the respective effective pixel areas, the presented sensitivity analysis does not consider pixel fill factors and assumes perfectly aligned pixels in a parallel X-ray beam. Neglecting the surface roughness of the pixels and the impact of air gaps, the fill factor η_f of the folded detector can be estimated as $\eta_f = d_{TCP}/(4d_{PEN} + d_{TCP})$ with d_{TCP} and d_{PEN} denoting the thickness of the TCP absorber and the PEN substrate, respectively

(see Fig. 1c). Note that the layer thicknesses of the other functional layers (e.g. electrodes, transport layers, and wires) are not considered at this stage. With substrate thicknesses of $d_{PEN} = 1.5\,\mu m$, the fill factor η_f would already be in the order of 50%. Consequently, a promising aspect for further research is to improve the fill factor of the folded detector by increasing the TCP absorber thickness and by utilizing thinner substrate foils.

Spatial resolution

For X-ray imaging detectors, the spatial resolution of a detector is a further important key performance indicator. Commonly, the spatial resolution of an X-ray imaging system is characterized by the modulation transfer function (MTF) that evaluates the signal transfer in the spatial frequency domain. In the specific case of only one relevant spatial dimension, the modulation transfer function MTF can be expressed by the edge spread function (ESF) that characterizes the system's response to a step input signal and can be evaluated as[21]

$$MTF(u) = \frac{\left|\mathcal{F}\left\{\frac{d}{dx}(ESF(x))\right\}\right|}{\mathcal{F}\left\{\frac{d}{dx}(ESF(x))\right\}\big|_{u=0}}, \qquad (2)$$

with the spatial frequency u, the position x, and the Fourier transform $\mathcal{F}$. In this study, we evaluate the presampled MTF of the folded detector by measuring the presampled ESF of an individual pixel. For this purpose, 150 kVp X-ray radiation and a movable 2-mm-thick tungsten edge placed in front of the folded detector are used (see Supplementary Fig. 5 for details on the experimental setup). The normalized pixel signal for different positions x of the tungsten edge represents measurements of the presampled edge spread function ESF(x) (see Supplementary Fig. 6a–c). Fig. 3c presents the presampled modulation transfer function MTF(u) of the folded detector. To this end, the measured edge spread function (see Supplementary Fig. 6c) is evaluated according to Eq. (2) based on a numerical and an analytical approach (see "Methods" for more details). The resulting presampled modulation transfer function MTF(u) shows a high performance with a value greater than 20 lp/mm at an MTF value of 0.2 typically used as a reference point to compare the spatial resolution of different X-ray imaging systems. Note that the presented analysis of the presampled modulation transfer function represents an evaluation of the spatial resolution that can potentially be reached with the folded detector design. The actually realized spatial resolution is additionally limited by aliasing effects due to the discrete sampling by the pixels of the detector. Aliasing effects are relevant if the presampled modulation transfer function has significant contributions from spatial frequencies larger than the cut-off frequency $u_c = 1/(2x_0)$ with x_0 denoting the sample spacing[22]. The sample spacing in the case of our folded detector is determined by the pixel pitch. Neglecting the surface roughness of the pixels and the impact of air gaps, the pixel pitch x_0 of our folded detector can be estimated as $x_0 = 4d_{PEN} + d_{TCP}$ with d_{PEN} and d_{TCP} denoting the thickness of the PEN substrate and the TCP absorber, respectively (see Fig. 1c). Note that similar to the estimation of the fill factor, the layer thicknesses of the other functional layers (e.g. electrodes, transport layers, and wires) are not considered at this stage. With a pixel pitch of $x_0 = 106\,\mu m$ and a corresponding cut-off frequency of $u_c = 4.7$ lp/mm, our proto-type detector cannot exploit the full potential regarding the spatial resolution. However, with a reduced susbtrate thickness of $d_{PEN} = 1.5\,\mu m$ and a corresponding cut-off frequency of $u_c = 41.7$ lp/mm the presented high spatial resolution of 20 lp/mm could already be fully exploited. This potentially reachable high spatial resolution outperforms the values recently reported for detectors based on MAPbBr$_3$, CsFAGA:Sr, a-Se, Cs$_2$AgBiBr$_6$, MA$_3$Bi$_2$I$_9$, and MAPbI$_3$ (see Table 1), with MA, FA, GA, and a-Se denoting methylammonium, formamidinium, guanidinium, and amorphous selenium.

Table 1. Spatial resolution reached with other X-ray absorbers.

X-ray absorber	Spatial resolution [lp/mm]	X-ray energy	Refs
MAPbBr$_3$	10	8 keV (peak energy)	[32]
CsFAGA:Sr	8.0	not specified	[33]
a-Se	7.1	30 kVp (tube voltage)	[34]
Cs$_2$AgBiBr$_6$	4.9	50 kVp (tube voltage)	[35]
MA$_3$Bi$_2$I$_9$	4.22	40 kVp (tube voltage)	[36]
MAPbI$_3$	3.5	70 kVp (tube voltage)	[37]
MAPbI$_3$	3.1, 3.83	100 kVp (tube voltage), 22 keV (energy at peak intensity)	[34,38]
TCP	20 (presampled)	150 kVp (tube voltage)	this work

The reported spatial resolutions refer to the spatial frequency at an modulation transfer function (MTF) value of 0.2. MA, FA, GA, a-Se, and TCP denote methylammonium, formamidinium, guanidinium, amorphous selenium, and triple cation perovskite, respectively.

Operational stability

A key aspect regarding the commercialization of a detector technology is the operational stability and lifetime of a device. In order to investigate the long-term behaviour of our folded detector, we measure the signal response of the folded device under continuous 150 kVp X-ray radiation (see Supplementary Fig. 7). Our device shows a highly stable response for more than 19 h of continuous X-ray radiation without any evidence of degradation. With a dose rate in air of $\dot{D}_{air} = 1.8$ mGy$_{air}$/s during the irradiation this corresponds to a stable detector response for a cumulative dose of $D_{air,cum} = 126.8$ Gy$_{air}$ which is equivalent to more than 422,000 chest radiographic examinations (Here, we assume a radiation exposure of 0.3 mGy$_{air}$ per examination[23]). It is worth mentioning that this experiment is performed under normal ambient conditions without any additional encapsulation. This indicates a high environmental stability of our detector. In conclusion, the demonstrated operational stability regarding radiation and environment-related impacts suggests a promising lifetime of our device making it attractive for commercialization. We speculate that the high operational stability of our device is a result of the utilized composition of the triple cation perovskite absorber and the used transport materials.

In summary, in this study, we have reported on the realization of an origami-inspired folded perovskite X-ray detector that combines a high X-ray sensitivity with the potential of an exceptional high spatial resolution. For this purpose, we have presented the design and fabrication of a foldable perovskite sensor array. The folded detector has shown a similar electrical functionality in the dark and a drastically increased detection performance under X-ray radiation compared to the planar device. By characterizing the sensor array under 50 kVp−150 kVp X-ray radiation, X-ray sensitivities in the range of 25−35 μC/(Gy$_{air}$cm^2) have been reached with the planar device, whereas remarkably higher X-ray sensitivities in the order of several hundred μC/ (Gy$_{air}$cm^2) and a record value of 1409 μC/(Gy$_{air}$cm^2) at 150 kVp have been achieved with the folded detector. This high detection performance has been reached without significant photoconductive gain and under zero external bias. Furthermore, we have demonstrated the potential of an exceptional high spatial resolution of the folded detector of more than 20 lp/mm under 150 kVp X-ray radiation. We have finally verified the operational stability of our device by showing a stable detector response for more than 19 h of continuous 150 kVp X-ray radiation and a cumulative dose of $D_{air,cum} = 126.8$ Gy$_{air}$. By having demonstrated a prototype of a folded perovskite X-ray detector with an

exceptional high performance, the results of this study represent a proof of concept of the folded device architecture. The concept can be extended for 2D array detectors by using stripe-like electrodes in the lateral direction.

Our work might pave the way for a generation of X-ray detectors with performance and cost advantages. An important aspect for further research that needs to be investigated is the noise of the folded detector. Through the use of thinner foils, a suitable patterning, and the integration of printed thin film transistors, a generation of low cost, folded large-area X-ray detector systems can evolve.

METHODS

X-ray detector fabrication

The sensor array (see Fig. 1 for the sensor layout) was fabricated on top of a 25-μm-thick polyethylene naphthalate (PEN) substrate foil (Teonex Q51). Prior to the device fabrication, a LPKF ProtoLaser R4 lasercutter was used to engrave folding lines in the PEN substrate foil. Subsequently, the PEN substrate foil was rinsed with isopropanol and then ultrasonically cleaned with acetone (10 min) and isopropanol (10 min). For all subsequent fabrication steps the PEN substrate foil was connected with dicing tape to an additional 125-μm-thick PEN carrier substrate (Teonex). Initially, a ≈ 75 nm-thick gold bottom electrode was thermally evaporated. Afterwards, a 15 nm-thick NiO_x hole transport layer was sputtered using a Pro Line PVD75 (Kurt J. Lesker Company), a deposition time of 450 s, a 1.3×10^{-3} mbar process pressure, Ar as process gas, 100 W, rf-conditions, and a NiO target (Kurt J. Lesker Company, 99.995% metallic purity). The base pressure in the chamber was $<10^{-7}$ mbar and the substrate was neither actively cooled nor heated during the deposition. The triple cation perovskite (TCP) absorber with a targeted composition of $Cs_{0.1}(FA_{0.83}MA_{0.17})_{0.9}Pb(Br_{0.17}I_{0.83})_3$ was then realized by digital inkjet printing as described in[24,25] (additionally a 2.4 vol% L-α-phosphatidylcholine (Sigma Aldrich) solution (0.5 mg/ml in DMSO) was added for processing reasons). Here, FA is formamidinium and MA is methylammonium. The printing frequency was $2-5$ kHz and the resolution was set to 2000 dpi. These printing parameters also ensure a suitable morphology of the perovskite absorber layer. Thereafter, an electron transport layer composed of 25 nmC_{60} fullerene (Sigma Aldrich 99.5%) and 3 nm bathocuproine (BCP) (Luminescence Technology) was thermally evaporated. Each pixel was finalized by thermally evaporated $\approx$75-nm-thick gold top electrodes. The effective area of the pixels in the planar configuration A_{planar} determined by the overlapping region of the top and the bottom electrodes with mean widths $\overline{w}_{t,b}$ can be estimated as $\overline{w}_b\overline{w}_t = 1.02$ mm $\times$ 2.17 mm $= 2.21$ mm^2. The electrical connection to the read out electronics was realized by aerosoljet-printed silver lines. For this purpose, 4 layers of silver were printed with an Aerosol Jet 5X System (Optomec, Inc.) using a silver dispersion ink (Sigma Aldrich, 736481), the Ultrasonic Decathlon (UA) system, a printing speed of 1 mm/s, a nozzle with a 600 μm diameter, a 200 sccm sheath gas flow rate, a 100 sccm atomizer flow rate, triethylene glycol monomethyl ether (TGME) as addback solvent, a solvent addback temperature of 29 °C, a cartridge temperature of 29 °C, an ultrasonic power of 530 mA, and a printing platform temperature of 100 °C. The silver lines were finally photonically sintered with a Pulseforge 1200 (Novacentrix) utilizing a voltage of 350 V, a pulse length of 200 μs, a repeat count of 150, and a fire rate of 2.0 Hz.

Electrical characterization in the dark and under X-ray radiation

The measurement of the detector current as a function of the applied voltage and as a function of time has been conducted with a Keithley 2450 SourceMeter source measure unit. The single pixels of the sensor array were sequentially addressed by an interconnected switching electronics. In the case of the X-ray sensitivity analysis a XT9160-DED X-ray tube (Viscom) equipped with a tungsten target and a 0.4-mm-thick aluminium filtration was used to generate X-ray irradiations with different intensities. The dose rate calibration was performed with a MagicMaX - rad/flu/dent dosimeter (IBA) equipped with a RQA semiconductor detector (IBA). A second setup equipped with a tungsten target XWT-225 microfocus X-ray tube (X-RAY WorX) was used to characterize the spatial resolution of the folded detector by the measurement of the edge spread function. This second setup was also used for the operational stability measurements. The dose rate calibration for the operational stability characterization was performed with the dosimeter equipment described above.

Sensitivity model

The theoretical X-ray sensitivity predictions S_{theo} utilized in this study rely on theoretical detector current densities J_{theo} and dose rates in air $\dot{D}_{air,theo}$ that were simulated by the following expression:

$$S_{theo} = \frac{J_{theo}}{\dot{D}_{air,theo}} = \frac{\int e\dot{\phi}_E\eta dE}{\int \dot{\phi}_E E\left(\frac{a_{en}}{\rho}\right)_{air} dE}, \tag{3}$$

with the elementary charge e, the spectral fluence rate of the incoming photons $\dot{\phi}_E$, the detector efficiency η, the photon energy E, and the mass energy absorption coefficient of air $(a_{en}/\rho)_{air}$. Following Eq. (3), the theoretical sensitivity predictions $S_{theo}(V_{tube})$ illustrated in Fig. 3a, b as a function of the X-ray tube voltage V_{tube} were calculated according to the following relation:

$$S_{theo}(V_{tube}) = \frac{\sum_i e\hat{\phi}(V_{tube}, E_i)\eta(E_i)}{\sum_i \hat{\phi}(V_{tube}, E_i)E_i\left(\frac{a_{en}}{\rho}\right)_{air}(E_i)}, \tag{4}$$

with the normalized X-ray spectrum $\hat{\phi}(V_{tube}, E_i)$. For this purpose, the SPEKTR 3.0 toolkit[26] was used to simulate the respective X-ray spectra (see Supplementary Fig. 8 for simulated X-ray spectra exemplarily shown for five X-ray tube voltages). The detector efficiency $\eta(E_i)$ and the mass energy absorption coefficients of air $(a_{en}/\rho)_{air}(E_i)$ were simulated and taken from our previously presented simulation framework[17]. To this end, an electric field of 0.13/6 V/μm (the built-in potential of 0.13 V has been taken from our previous study[18] and the TCP layer thickness of 6 μm was determined by white light interferometry (see Supplementary Fig. 9a, b)), a gold top electrode for the planar device with a thickness of 75 nm, an active folding length for the folded detector of 2.1656 mm, a TCP density of 3.75 g/cm^3 (estimated by the mass of the printed TCP and the respective volume (see Supplementary Fig. 9c, d)), an electron–hole pair creation energy in the range of $4.0-5.5$ eV (estimated according to[27–29] with the TCP band gap taken from ref. [30]), and a mobility lifetime product of 2×10^{-6} cm^2/V[18] were assumed. Note that the stated mobility lifetime product is assumed for both electrons and holes.

Modulation transfer function

The modulation transfer function MTF(u) in this study was determined according to Eq. (2). For this purpose, the derivative and the Fourier transform of the measured edge spread function ESF(x) (see Supplementary Fig. 6c) were evaluated by a numerical and an analytical approach. In the case of the numerical evaluation, the derivative of the edge spread function $\frac{d}{dx}(ESF(x))$ was numerically calculated leading to the line spread function LSF(x) shown in Supplementary Fig. 6d. Subsequently, the discrete Fourier transform $\mathcal{F}(LSF(x))$ was evaluated by a Fast Fourier transform algorithm implemented in MATLAB. In the case of the analytical evaluation, the analytical edge spread function and the corresponding analytically derived modulation transfer function presented in[31]

were used. For this purpose, the edge spread function introduced in ref. [31] was fitted to the measured data shown in Supplementary Fig. 6c and the resulting function coefficients were used to evaluate the analytical modulation transfer function.

DATA AVAILABILITY

The data presented in this study are available from the corresponding author on reasonable request.

CODE AVAILABILITY

The code used to analyse and generate the data presented in this study is available from the corresponding author on reasonable request.

REFERENCES

1. Kalender, W. A. X-ray computed tomography. *Phys. Med. Biol.* **51**, R29–R43 (2006).
2. Spahn, M. X-ray detectors in medical imaging. *Nucl. Instrum. Methods Phys. Res. A: Accelerators Spectrometers Detectors Assoc. Equipment* **731**, 57–63 (2013).
3. Kotwaliwale, N. et al. X-ray imaging methods for internal quality evaluation of agricultural produce. *J. Food Sci. Technol.* **51**, 1–15 (2014).
4. De Chiffre, L., Carmignato, S., Kruth, J.-P., Schmitt, R. & Weckenmann, A. Industrial applications of computed tomography. *CIRP Annals* **63**, 655–677 (2014).
5. Bunaciu, A. A., gabriela Udriştioiu, E. & Aboul-Enein, H. Y. X-ray diffraction: instrumentation and applications. *Crit. Rev. Anal. Chem.* **45**, 289–299 (2015).
6. van de Kamp, T. et al. Evolution of flexible biting in hyperdiverse parasitoid wasps. *Proc. R. Soc. B: Biol. Sci.* **289**, 1–9 (2022).
7. He, Y., Hadar, I. & Kanatzidis, M. G. Detecting ionizing radiation using halide perovskite semiconductors processed through solution and alternative methods. *Nat. Photonics* **16**, 14–26 (2022).
8. Basiricò, L., Ciavatti, A. & Fraboni, B. Solution-grown organic and perovskite x-ray detectors: a new paradigm for the direct detection of ionizing radiation. *Adv. Mater. Technol.* **6**, 2000475 (2020).
9. Zhou, Y., Chen, J., Bakr, O. M. & Mohammed, O. F. Metal halide perovskites for X-ray imaging scintillators and detectors. *ACS Energy Lett.* **6**, 739–768 (2021).
10. Kakavelakis, G. et al. Metal halide perovskites for high-energy radiation detection. *Adv. Sci.* **7**, 2002098 (2020).
11. Wei, H. & Huang, J. Halide lead perovskites for ionizing radiation detection. *Nat. Commun.* **10**, 1066 (2019).
12. Li, C. et al. Ultrafast and broadband photodetectors based on a perovskite/organic bulk heterojunction for large-dynamic-range imaging. *Light: Sci. Appl.* **9**, 31 (2020).
13. Morteza Najarian, A. et al. Sub-millimetre light detection and ranging using perovskites. *Nat. Electron.* **5**, 511–518 (2022).
14. Yao, M. et al. High-temperature stable FAPbBr3 single crystals for sensitive X-ray and visible light detection toward space. *Nano Lett.* **21**, 3947–3955 (2021).
15. Gu, Y. et al. Study of a high-resolution, 3D positioning cadmium zinc telluride detector for PET. *Phys. Med. Biol.* **56**, 1563–1584 (2011).
16. Liu, X., Grönberg, F., Sjölin, M., Karlsson, S. & Danielsson, M. Count rate performance of a silicon-strip detector for photon-counting spectral CT. *Nucl. Instrum. Methods Phys. Res. A: Accelerators Spectrometers Detectors Associated Equipment* **827**, 102–106 (2016).
17. Mescher, H., Hamann, E. & Lemmer, U. Simulation and design of folded perovskite x-ray detectors. *Sci. Rep.* **9**, 5231 (2019).
18. Mescher, H. et al. Flexible inkjet-printed triple cation perovskite X-ray detectors. *ACS Appl. Mater. Interfaces* **12**, 15774–15784 (2020).
19. Kasap, S. O. X-ray sensitivity of photoconductors: application to stabilized a-Se. *J. Phys. D: Appl. Phys.* **33**, 2853–2865 (2000).
20. Pan, Z., Wu, L., Jiang, J., Shen, L. & Yao, K. Searching for high-quality halide perovskite single crystals toward X-ray detection. *J. Phys. Chem. Lett.* **13**, 2851–2861 (2022).
21. Boreman, G. D. MTF Measurement methods. In: *Modulation Transfer Function in Optical and Electro-Optical Systems*, Chapter 4, 69–84 (SPIE, 2001). http://ebooks.spiedigitallibrary.org/content.aspx?doi=10.1117/3.419857.ch4.
22. Cunningham, I. Applied linear-systems theory. In: *Handbook of Medical Imaging, Volume 1. Physics and Psychophysics*, 79–159 (SPIE, 2000). http://ebooks.spiedigitallibrary.org/content.aspx?doi=10.1117/3.832716.ch2.
23. Heilmaier, C., Zuber, N. & Weishaupt, D. Implementation of a patient dose monitoring system in conventional digital X-ray imaging: initial experiences. *Eur. Radiol.* **27**, 1021–1031 (2017).
24. Schackmar, F. et al. Perovskite solar cells with all-inkjet-printed absorber and charge transport layers. *Adv. Mater. Technol.* **6**, 2000271 (2021).
25. Eggers, H. et al. Inkjet-printed micrometer-thick perovskite solar cells with large columnar grains. *Adv. Energy Mater.* **10**, 1903184 (2020).
26. Punnoose, J., Xu, J., Sisniega, A., Zbijewski, W. & Siewerdsen, J. H. Technical Note: <scp>spektr</scp> 3.0-A computational tool for x-ray spectrum modeling and analysis. *Med. Phys.* **43**, 4711–4717 (2016).
27. Devanathan, R., Corrales, L. R., Gao, F. & Weber, W. J. Signal variance in gamma-ray detectors—a review. *Nucl. Instrum. Methods Phys. Res. A: Accelerators Spectrometers Detectors Associated Equipment* **565**, 637–649 (2006).
28. Klein, C. A. Bandgap dependence and related features of radiation ionization energies in semiconductors. *J. Appl. Phys.* **39**, 2029–2038 (1968).
29. Que, W. & Rowlands, J. A. X-ray photogeneration in amorphous selenium: geminate versus columnar recombination. *Phys. Rev. B* **51**, 10500–10507 (1995).
30. Tosado, G. A., Lin, Y. Y., Zheng, E. & Yu, Q. Impact of cesium on the phase and device stability of triple cation Pb-Sn double halide perovskite films and solar cells. *J. Mater. Chem. A* **6**, 17426–17436 (2018).
31. Boone, J. M. & Seibert, J. A. An analytical edge spread function model for computer fitting and subsequent calculation of the LSF and MTF. *Med. Phys.* **21**, 1541–1545 (1994).
32. Wei, W. et al. Monolithic integration of hybrid perovskite single crystals with heterogenous substrate for highly sensitive X-ray imaging. *Nat. Photonics* **11**, 315–321 (2017).
33. Jiang, J. et al. Synergistic strain engineering of perovskite single crystals for highly stable and sensitive X-ray detectors with low-bias imaging and monitoring. *Nat. Photonics* **16**, 575–581 (2022).
34. Kim, Y. C. et al. Printable organometallic perovskite enables large-area, low-dose X-ray imaging. *Nature* **550**, 87–91 (2017).
35. Yang, B. et al. Heteroepitaxial passivation of Cs2AgBiBr6 wafers with suppressed ionic migration for X-ray imaging. *Nat. Commun.* **10**, 1989 (2019).
36. Liu, Y. et al. Large lead-free perovskite single crystal for high-performance coplanar X-ray imaging applications. *Adv. Opt. Mater.* **8**, 2000814 (2020).
37. Deumel, S. et al. High-sensitivity high-resolution X-ray imaging with soft-sintered metal halide perovskites. *Nat. Electron.* **4**, 681–688 (2021).
38. Song, Y. et al. Elimination of interfacial-electrochemical-reaction-induced polarization in perovskite single crystals for ultrasensitive and stable X-ray detector arrays. *Adv. Mater.* **33**, 2103078 (2021).

AUTHOR CONTRIBUTIONS

H.M. designed this study, fabricated the detector, performed most of the measurements and characterizations, analysed the data, interpreted the results, and wrote the first draft of the manuscript. F.S. and H.M. inkjet-printed the TCP absorber. F.S. fabricated reference samples for the surface characterization and performed a part of the white light interferometry. Q.Z. and G.G. contributed with their expertise on white light interferometry. R.H. and H.M. aerosoljet-printed and photonically sintered the silver lines. H.E. contributed with his expertise on inkjet printing and laser cutting. M.Z., E.H., and H.M. performed and analysed the measurements of the spatial resolution and the operational stability. E.H. and H.M. conducted the computed tomography of the folded detector. M.Z. and E.H. contributed with their profound knowledge on X-ray physics and technologies. G.G. and H.M. performed the engraving and the cutting with the laser cutter. G.G., R.H., and H.M. three-dimensional printed the sample holders for the detector. J.D. and H.M. designed and realized the switching electronics to address the pixels of the detector. A.G.R. contributed to the evaluation of the data and to the interpretation of the results. T.Z., G.H.-S., U.W.P., and U.L. supervised the entire study. All authors contributed to the manuscript.

COMPETING INTERESTS

The authors declare no competing interests.

ADDITIONAL INFORMATION

Supplementary information The online version contains supplementary material available at https://doi.org/10.1038/s41528-023-00240-9.

Correspondence and requests for materials should be addressed to Uli Lemmer.

Reprints and permission information is available at http://www.nature.com/reprints

Publisher's note Springer Nature remains neutral with regard to jurisdictional claims in published maps and institutional affiliations.